Research Article | Vol. 12, No. 7 / 1 Jul 2022 / Optical Materials Express 2474
Optical Materials EXPRESS

Realization of tunable dual-type quasi-bound states in the continuum based on a Dirac semimetal metasurface

HANG LIU, JINGXIANG GAO, HUIYUN ZHANG, AND YUPING ZHANG*

College of Electronics and Information Engineering, Shandong University of Science and Technology, Qingdao 266510, China
*sdust_thz@163.com

Abstract: In this study, two types of tunable quasi-bound states in the continuum (BIC) based on Dirac semimetal metamaterial (DSM) in the terahertz (THz) band are proposed in the same metasurface. The symmetry-protected BICs are achieved by altering the structural symmetry. The accidental BICs are realized by adjusting the structural parameters, and the quality factor (Q factor) of the corresponding quasi-BICs can be as high as 175. To better understand the excitation mechanism of the quasi-BIC, we investigated the magnetic field distribution and current distribution of the BIC and quasi-BIC, respectively. The results showed that the accidental BIC and the symmetry-protected BIC have a common resonance mode, and the two LC resonance modes are coupled with each other, which causes a strong resonance. The dynamic modulation of the transmission amplitude is achieved by changing the Fermi energy of the DSM at a nearly constant resonant frequency, and the difference in amplitude modulation is about 46%. Based on the idea of amplitude modulation, the design of the Dirac semimetal film (DSF) metasurface array for stereoscopic graphic display is realized.

1. Introduction

A high Q factor is pursued in optical resonators, which must strongly enhance the interaction between electromagnetic radiation and matter. Resonators with strong interactions have the ability to excite several specific physical phenomena and are valuable for extremely important applications in sensitive sensors [1–3], nonlinear enhancement [4,5], filters [6,7], lasers [8,9] and perfect absorption [10]. The BIC [11,12] is a localized state in the continuous spectrum, that lies within the light cone and provides perfect localization. Ideally, BIC have an infinite Q factor and zero resonance linewidth, as well as an infinite lifetime and zero leakage. Therefore, they are hidden in the normal propagating electromagnetic spectrum and are not detected. However, the BIC can be coupled to the extended state by adding a perturbation to the resonator structure, resulting in a finite narrow bandwidth and a high Q factor leakage mode (i.e., quasi-BIC) that can be identified. Quasi-BIC is usually achieved in two ways: symmetry breaking of the symmetry-protected BIC [13] and parameter modulation of the accidental BIC [14,15]. In photonics, symmetry-protected BIC and accidental BIC have been implemented in coupled waveguides [16], photonic crystals [17], photonic circuits [18,19], and metasurface [20]. In particular, the BIC based on metasurface can effectively control the radiation damping rate [21], which paves the way for the exploration of high Q factor.

The application [22–26] of metasurface-based BIC in THz band has been intensively studied in recent years. Liu *et al.* [25] achieved quasi-BIC with a high Q factor in metallic resonators. Han *et al.* [26] achieved a quasi-BIC by breaking the C_2 symmetry of the dielectric metasurface, and the Q factor was increased by several orders of magnitude. Nevertheless, most of these devices are consist of metallic or all-dielectric resonators tuned to different bands by careful optimization of the geometrical properties, which severely restricts certain applications. Recently, much research

#463585 https://doi.org/10.1364/OME.463585
Journal © 2022 Received 10 May 2022; revised 30 May 2022; accepted 30 May 2022; published 7 Jun 2022

Optical Materials EXPRESS

has been done in the field of functional metasurface [27] to achieve dynamic tuning of the working wavelengths of BICs through optically active materials, including integrated liquid crystals, temperature-sensitive materials, photosensitive materials, and graphene. Elena Mikheeva *et al.* [28] fabricated tunable quasi-BIC devices using photosensitive chalcogenide glass materials, but they are susceptable to oxidation and require high light intensity. Chen *et al.* [29] used graphene and strontium titanate materials to create a THz metasurface that enables tunable quasi-BIC by independently changing the Fermi energy of the graphene and the temperature of the strontium titanate material. However, the graphene is thin and interacts only weakly with the incident radiation. Fortunately, DSM is a topological semimetal, a new type of quantum material with a similar energy band structure to graphene, also known as "three-dimensional graphene". By dynamically altering the Fermi energy with an applied bias voltage, DSM can change its conductivity from "dielectric" to "semimetallic" to "metallic". Research exploiting the tunable properties of Dirac semimetals has also begun to attract considerable interest. In the THz band, Wang's group proposed the tunable absorber [30], the bandpass filter [31], and the tunable BIC in bulk Dirac semimetal metasurface [32,33], etc. Zhang's group proposed tunable electromagnetically induced transparency [34,35], polarization converter [36], etc. In optical applications, the level of the Q factor directly affects the performance of the device. Although the above work has achieved various tuning functions using active materials, there are few investigations into the tuning of BICs with naturally high Q factors. Therefore, it is interesting to incorporate DSM into the metasurface to achieve a dynamically tunable BIC.

In this research, we propose a metasurface model for optical modulator-based quasi-BIC using DSM, in which the unit cell of the metasurface consists of 'T-I' shaped resonator pair (T-ISRP). Due to the special characteristics of this structure with C_2 symmetry and parameter modulation, it can realize two types of BIC in the THz band: symmetry-protected BIC and accidental BIC. The Q factor of the quasi-BIC and the radiation loss of the system can be controlled if both zero-leakage BIC can be degraded to quasi-BIC with a high Q factor by modifying the structural parameters of the metasurface or the asymmetry parameters. On the DSF metasurface, the resonant mechanism is investigated by simulating the surface current distribution and the electric and magnetic field distribution. Interestingly, at nearly constant resonant frequency, we achieve independent control of the transmission amplitude of the quasi-BIC and dynamic modulation of the Q factor by adjusting the Fermi energy of the DSF metasurface, as well as an amplitude modulation difference of about 46% at a transmission amplitude of about 80%. Based on the principle of independent modulation of the quasi-BIC amplitude, we have developed a dynamic display function for in-plane stereo patterns that dramatically extends the scope of metasurface applications. The display function is dynamic because the resonance peak of the quasi-BIC state of each pixel can be adjusted at random. Thus, any desired stereo image can be displayed by the DSF metasurface array, which is not possible with two-dimensional imaging of the BIC switch [37].

2. Design and theory

We have designed a unit cell of a tunable DSF metasurface as shown in Fig. 1(a), which consists of a two-layer structure with a Dirac semimetallic metasurface T-ISRP on the top layer and lossless high-refractive index silicon on the substrate. Silicon has a dielectric constant of 11.9 and a thickness t_2 of 15 μm. Figure 1(b) shows a top view of the unit cell. The width ω of the T-ISRP is 18 μm and its thickness t_1 of 0.2 μm. The period P of the unit structure in the figure is 150 μm. The distance between the 'T' shaped resonator pair (TSRP) is d, and d is a varying quantity. The initial length of the 'I' bar is $l_1 = l_2 = 86$ μm, the length l_2 of the right 'I' bar varies in the range of 59-113 μm, and the T-ISRP always remains symmetrical about the x-axis. Full-wave simulation of the designed metasurface is performed using the frequency domain solver of CST Microwave Studio, and the metasurface is calculated numerically using TE wave with y-polarization positive

Optical Materials EXPRESS

incidence. Periodic boundary conditions are applied to the x and y directions of the unit cell, and open boundary conditions are applied to the z direction.

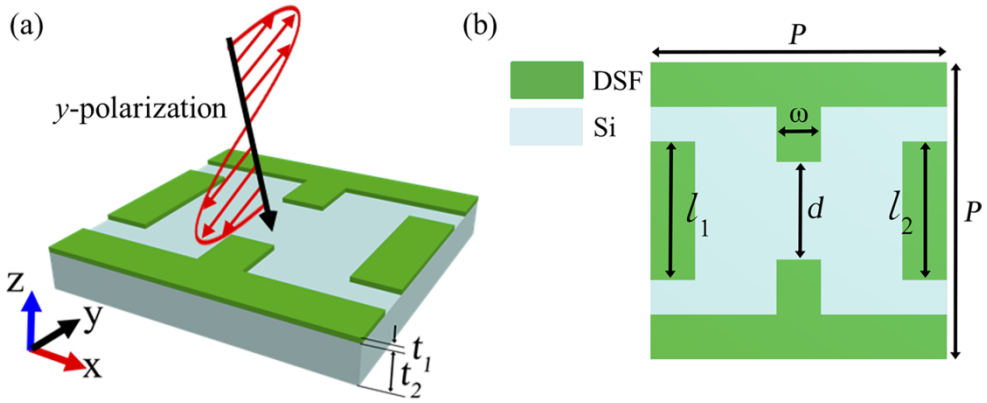

Fig. 1. Schematic diagram for the proposed DSF metasurface (a) stereo view and (b) top view.

According to the stochastic phase approximation theory, in the low-temperature limit , the dynamic conductivity of the 3D Dirac semimetal using the Kubo formula is expressed as [30,38]:

$$\mathrm{Re}\sigma(\Omega) = \frac{e^2}{\hbar}\frac{gk_F}{24\pi}\Omega\theta(\Omega - 2) \tag{1}$$

$$\mathrm{Im}\sigma(\Omega) = \frac{e^2}{\hbar}\frac{gk_F}{24\pi^2}\left[\frac{4}{\Omega} - \Omega\ln\left(\frac{4\varepsilon_c^2}{|\Omega^2 - 4|}\right)\right] \tag{2}$$

where, e is the electron charge, $\hbar$ is the approximate Planck constant, $k_F = E_F/\hbar v_F$ is the Fermi momentum, $\Omega = \hbar\omega/E_F + i\hbar\tau^{-1}/E_F$, E_F is the Fermi energy, $\tau = \mu E_F/ev_F^2$ is the relaxation time, $\mu = 3 \times 10^4 cm^2V^{-1}s^{-1}$, θ is the Riemann-Siegel function, $v_F = 10^6 m/s$ is the Fermi velocity. In this study, we have chosen AlCuFe quasicrystals as the 3D Dirac semimetals, $g = 40$ is the degeneracy factor. The complex relative permittivity of 3D Dirac semimetals can be expressed as [39,40]:

$$\varepsilon = \varepsilon_b + i\sigma/\omega\varepsilon_0 \tag{3}$$

where, $\varepsilon_b = 1$, ε_0 is the vacuum dielectric constant. In the simulation, we calculate the values of different Fermi's dielectric constants using MATLAB software at THz band based on the relationship between the properties of DSM and electromagnetic waves, and then import the corresponding dielectric constants into the simulation software to achieve the setting of DSM.

3. Results and discussion

First, we investigate the accidental BIC's excitation process and the effect of the structural parameters on the Q factor by keeping Fermi energy of the DSF ($E_f = 0.5$ eV) and adjusting the TSRP spacing d while maintaining the structural symmetry between the T-ISRP. Figure 2(a) shows the spacing d of the TSRP and the incident wave frequency as a function of the transmission amplitude. It can be seen that the resonance band becomes narrower as the distance d increases, and when d = 40 μm, the resonance in the electromagnetic spectrum disappears and shows a dark state BIC (black circles in Fig. 2(a)) with zero radiation due to the destructive interference of the modes, and then the resonance band starts to broaden. At d = 40 μm, regardless of whether the structural parameter d increases or decreases, the phase mismatch between the modes causes the energy to be radiated, resulting in a quasi-BIC with finite bandwidth and finite lifetime, whose

Optical Materials EXPRESS

resonant frequency gradually blueshifts. The process of continuous tuning of the parameters confirms that it is an accidental BIC. In Fig. 2(b) the resonant frequency and Q factor are plotted as a function of the TSRP spacing d. The Q factor is defined as [25]:

$$Q = f_{peak}/(f_{peak} - f_{dip}) \tag{4}$$

where f_{peak} is the resonant peak frequency and f_{dip} is the resonant dip frequency of the quasi-BIC. From the figure, it can be seen that the resonant peak frequency of the quasi-BIC gradually blueshifts as the spacing d increases, the modulation range is about 0.2 THz, and the Q factor gradually increases. At d = 40 μm, the radiation leakage from the bound state is zero, resulting in an infinite resonance amplitude and a linewidth of zero. Therefore, the Q factor of this BIC reaches its maximum and shows an infinite lifetime. Subsequently, the Q factor shows a decreasing trend, and at d = 42 μm, the BIC degenerates to a quasi-BIC with a Q factor of about 175.

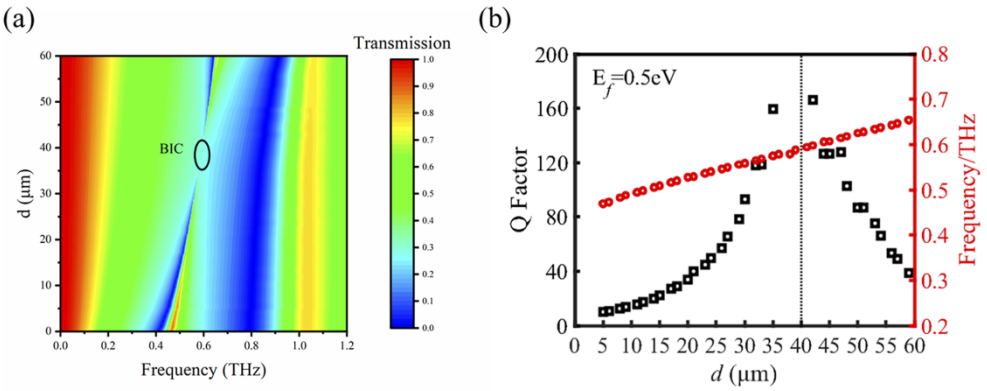

Fig. 2. (a) Transmission amplitude as a function of TSRP spacing and incident THz wave frequency. (b) Variation of the Q factor and resonant frequency as a function of spacing.

To better understand the excitation mechanism of the quasi-BIC, we investigated the magnetic field distribution and current distribution of the BIC and quasi-BIC, respectively. Since the quasi-BIC is more observable with a relatively high Q factor, we chose the magnetic field versus current distribution at the resonant peak frequency $f_1 = 0.5724$ THz for the quasi-BIC at d = 34 μm versus the resonant peak frequency $f_2 = 0.58$ THz for the BIC at d = 40 μm, as shown in Fig. 3. And Fig. 3(b) shows the magnetic field distribution in the z-direction for $f_1 = 0.5724$ THz and $f_2 = 0.58$ THz. Electromagnetic waves transfer energy mainly in the z-axis direction in the BIC state, therefore the magnetic field direction is in the xy-plane. However, in the quasi-BIC state, the energy transfer is not limited to the z-axis direction due to energy losses, which means that part of the magnetic field is generated outside the xy plane. At the resonant frequency of $f_1 = 0.5724$ THz, a remarkable magnetic field loss is observed due to the magnetic field distribution compared to the resonance of the BIC in the dark state. Figure 3(c) shows the current density vector distributions of the quasi-BIC and the BIC in the z-direction of the DSF metasurface. As can be seen from the figure, the current distribution at f_1 shows two co-directional LC resonant modes coupled together and causing a strong resonance in the common radiation channel, and the electromagnetic spectrum shows a quasi-BIC of the Fano linear type [20], which is a radiation mode with a high Q factor of about 150. When the spacing d of the TSRP varies to 40 μm, the current distribution at the corresponding f_2 shows an electric dipole resonance mode with three current directions flowing along the bar from top to bottom, and the blue curve in Fig. 3(a) shows a dark state BIC with an infinite Q factor due to the destructive interference between the modes, resulting in radiation elimination.

Optical Materials EXPRESS

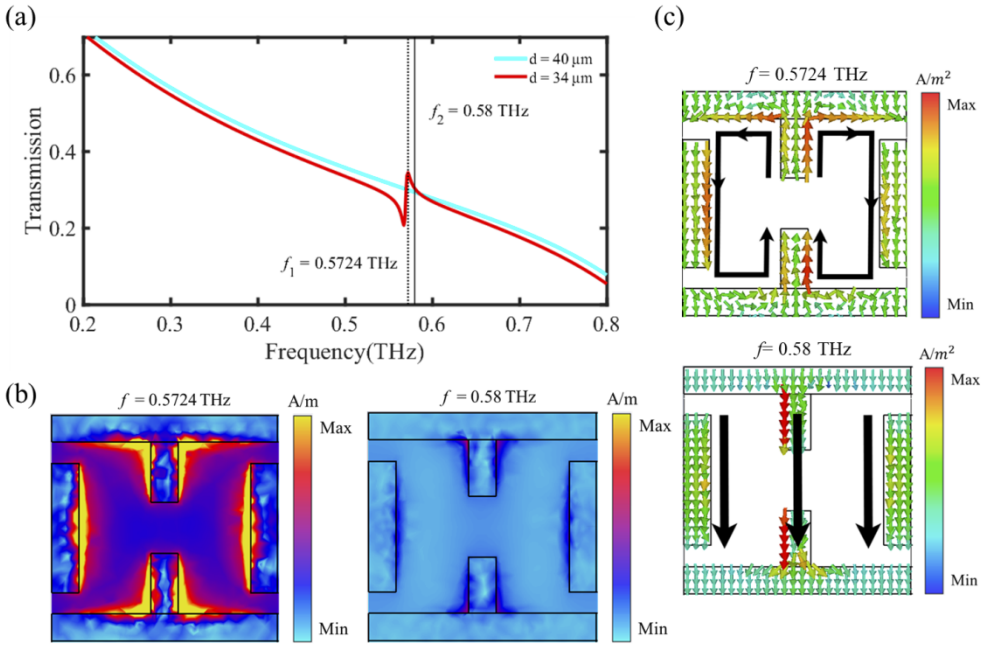

Fig. 3. Quasi-BIC and BIC (a) transmission spectrum. (b) Magnetic field distribution in the z direction. (c) Current distribution in the z-direction.

The excitation process of the accidental BIC has been analyzed above, and we also have observed a symmetry-protected BIC due to the C_2 rotational and mirror symmetry of the DSF metasurface. To analyze the symmetry-protected BIC, we adjusted the structural parameters by changing the length l_2 (the variation of l_2 ranges from 59-113 μm) of the right 'I' bar of the DSF metasurface structure while keeping d = 40 μm constant, which resulted in the breaking of C_2 symmetry on the DSF metasurface. The top view of the structure after changing the symmetry of the DSF metasurface is shown in Fig. 4(a). The asymmetry parameter is defined as:

$$\alpha = (l_1 - l_2)/l_2 \tag{5}$$

where l_1 is the length of the left 'I' bar, l_2 is the length of the right 'I' bar, α is a dimensionless parameter. Figure 4(b) shows the transmission amplitude of the DSF metasurface as a function of the asymmetric parameters and incident wave frequency. When $l_2 = l_1 = 86$ μm, i.e., α = 0, the symmetry of the DSF metasurface structure remains intact, and the transmission spectrum exhibits the ideal dark state BIC (black circle in Fig. 4(b)) with an infinite Q factor. When α ≠ 0, the C_2 symmetry of the structure is broken, leading to energy leakage from the bound state and coupling with the incident wave resulting in a quasi-BIC. We can see that the type of BIC is strongly dependent on the symmetry of the structure and can therefore be classified as a symmetry-protected BIC. When $l_2 < l_1$, i.e., α < 0, the transmission amplitude of the quasi-BIC is relatively small, as shown in Fig. 4(b), but the Q factor is quite high and remains above 100, as shown in Fig. 4(c) for the relationship between the asymmetry parameter and the Q factor. When $l_2 > l_1$, i.e., α > 0, the transmission amplitude increases significantly with the increase of the asymmetry parameter, and the resonant frequency gradually red shifts. In general, the Q factor increases gradually with the decrease of the absolute value of the structural asymmetry parameter, until l_2 is near 86 μm, because the symmetry of the structure has a small perturbation, resulting in a very small energy loss from the bound state and the corresponding Q factor tends to infinity. Therefore, we still have difficulty observing the changes in the electromagnetic

Optical Materials EXPRESS

spectrum corresponding to the conversion of the BIC to a quasi-BIC. We also examined the current distribution between the symmetry-protected BIC and the degenerate quasi-BIC, and found that the distribution is the same as in Fig. 3(c). When the quasi-BIC is converted to the BIC, the LC mode disappears completely and the dipole mode remains unchanged.The coupling between the leaked energy and the incident wave disappears due to the symmetry of the DSF metasurface structure, which eliminates the sharp resonance.

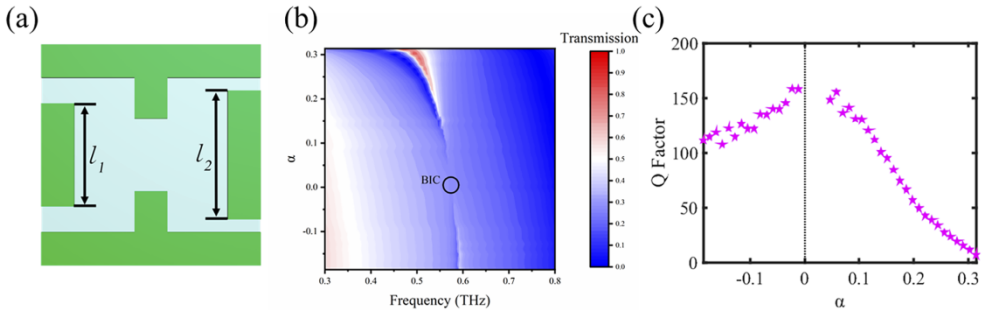

Fig. 4. (a) Top view of the metasurface unit cell for 'I' bar length l_2 variation. (b) Transmission amplitude of the symmetry-protected BIC as a function of asymmetry parameter and incident wave frequency. (c) Relationship between the asymmetry parameter and the Q factor.

From the above data analysis, it can be seen that both approaches can achieve dark state BIC and quasi-BIC with a high Q factor, with the Q factor of the quasi-BIC being slightly higher after degradation of the accidental BIC. So far, the function of most devices for metasurface applications is uniquely determined after the structural parameters are set. If we want to change the performance of the device, we need to modify the parameters and composition form of the metasurface unit cell, and it needs to be redesigned and reprocessed, which limits the application of the device. To investigate the amplitude tunability of T-ISRP, we take the accidental BIC as an example and numerically simulate the transmission spectra of the DSF metasurface at different Fermi energies.

Here, we take $l_2 = l_1 = 86$ μm, d = 25 μm and change the Fermi energy of the DSF metasurface by applying a gate bias voltage [41] to achieve the active modulation of the quasi-BIC, as shown in Fig. 5. It can be seen that the transmission amplitude gradually increases with increasing Fermi energy, while the resonant frequency remains almost constant, as shown in Fig. 5(a). To analyze the tuning mechanism of the transmission amplitude, we plotted the Fermi energy and incident wave frequency as a function of the real and imaginary parts of the complex refractive index of the DSM and the distribution of the electric field of the resonance peak frequency, as shown in Fig. 5(b) and Fig. 5(c), respectively. From Fig. 5(b), it can be seen that at $f = 0.5424$ THz, the real part of the complex refractive index hardly changes with the increase of the Fermi energy, so the resonance frequency remains almost unchanged, while the imaginary part of the complex refractive index increases with the increase of the Fermi energy, resulting in an enhancement of the resonance intensity. The electromagnetic spectrum has a low amplitude of the quasi-BIC when the total electric field at $E_f = 0.05$ eV is relatively weak, as shown in Fig. 5(c). When the Fermi energy increases to 0.55 eV, the total electric field of the T-ISRP is enhanced, leading to an increase in the resonance current, so that the absolute intensity of the transmission changes significantly. Essentially, the change in the DSM dielectric constant in Fig. 5(b) causes this phenomenon, so that the transmission amplitude of the quasi-BIC gradually increases with the increase of the Fermi energy at an almost constant resonant frequency.

Optical Materials EXPRESS

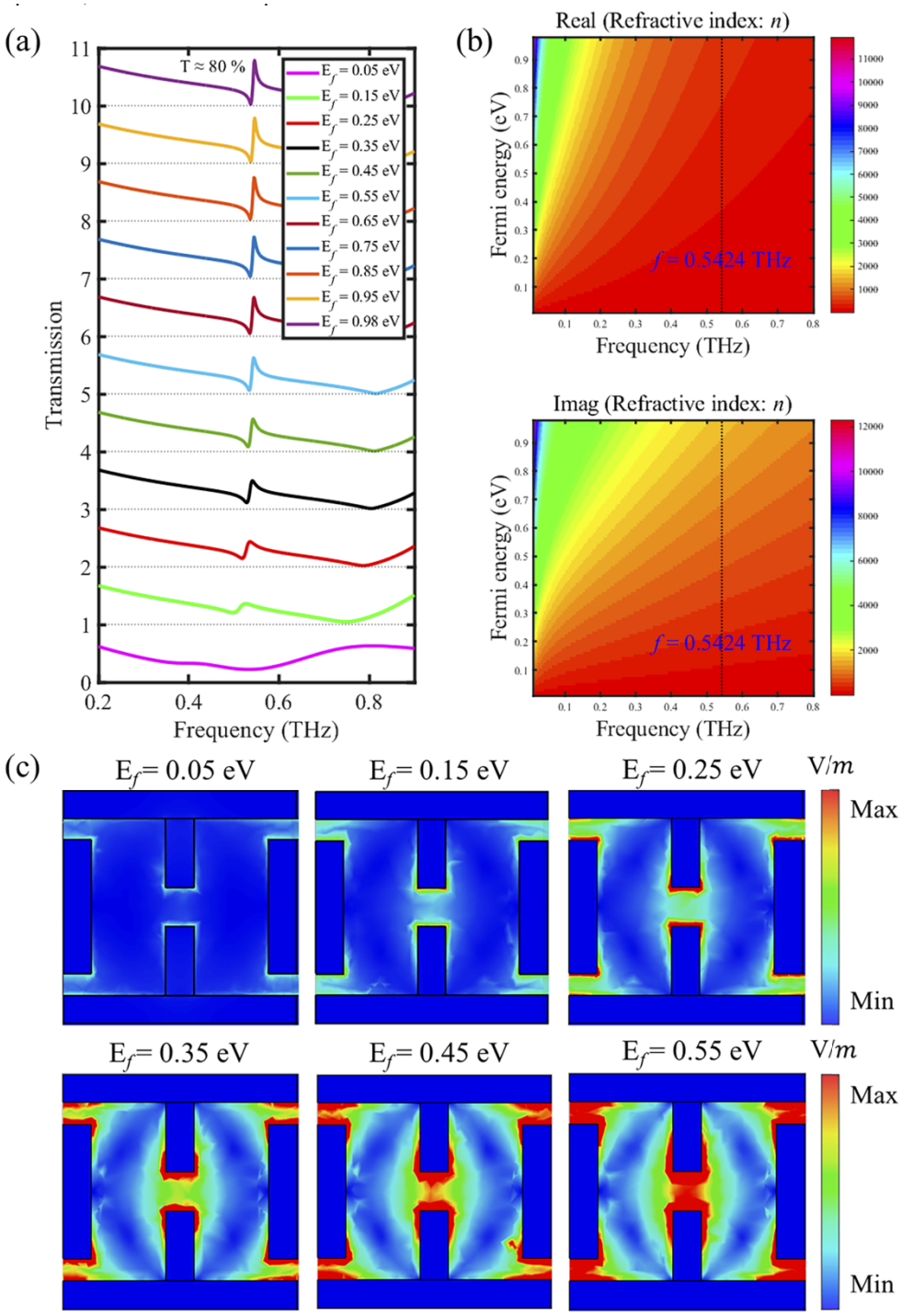

Fig. 5. (a) The transmission spectrum of DSF as a function of Fermi energy and incident wave frequency. (b) The real and imaginary parts of the complex refractive index of DSM. (c) The electric field distribution of Quasi-BIC states at Fermi energies of 0.05 eV, 0.15 eV, 0.25 eV, 0.35 eV, 0.45 eV, and 0.55 eV, respectively.

Optical Materials EXPRESS

To quantify the modulation effect of the variation of the Fermi energy on the transmission amplitude, we define the amplitude modulation difference as:

$$\Delta T_{MAX} = (T - T_0) \times 100\% \tag{6}$$

where T_0 is the amplitude of the resonance peak of the quasi-BIC at $E_f = 0.05$ eV and T is the amplitude of the resonance peak of the quasi-BIC at different Fermi energies. Figure 6(a) shows the amplitude modulation difference and Q factor as a function of the Fermi energy of the DSM. It can be seen that the amplitude at $E_f = 0.98$ eV modulates by about 46% compared to the transmission amplitude at $E_f = 0.05$ eV. And the quasi-BIC in the red circle in Fig. 5(a) transmits about 80% of the light, which improves the clarity of the image representation of the DSF metasurface coded array designed later in this study. Meanwhile, the Q factor increases with increasing Fermi energy, by approximately 60 in the range of 0.35-0.98 eV change in Fermi energy. The amplitude of the quasi-BIC is dynamically modulated by the DSM, as shown in Figs. 5(a) and 6(a). Thus the mechanism of the dynamic modulation of amplitude of the quasi-BIC can be used to develop a digital encoding-like metasurface. With constant structural parameters, the modulation range of the Fermi energy of the DSM with amplitude modulation difference and relatively large Q factor is 0.35-0.98 eV, and the transmission amplitude of the quasi-BIC is actively modulated by adjusting the Fermi energy of multiple DSF metasurface unit cells, and different transmission amplitudes can correspond to different chromaticities to represent the intensity of image colors. Compared to the patterns or digital planar graphics displayed by switching between quasi-BIC and BIC [37], our DSF metasurface array is more advantageous because it can dynamically display planar stereoscopic graphics.

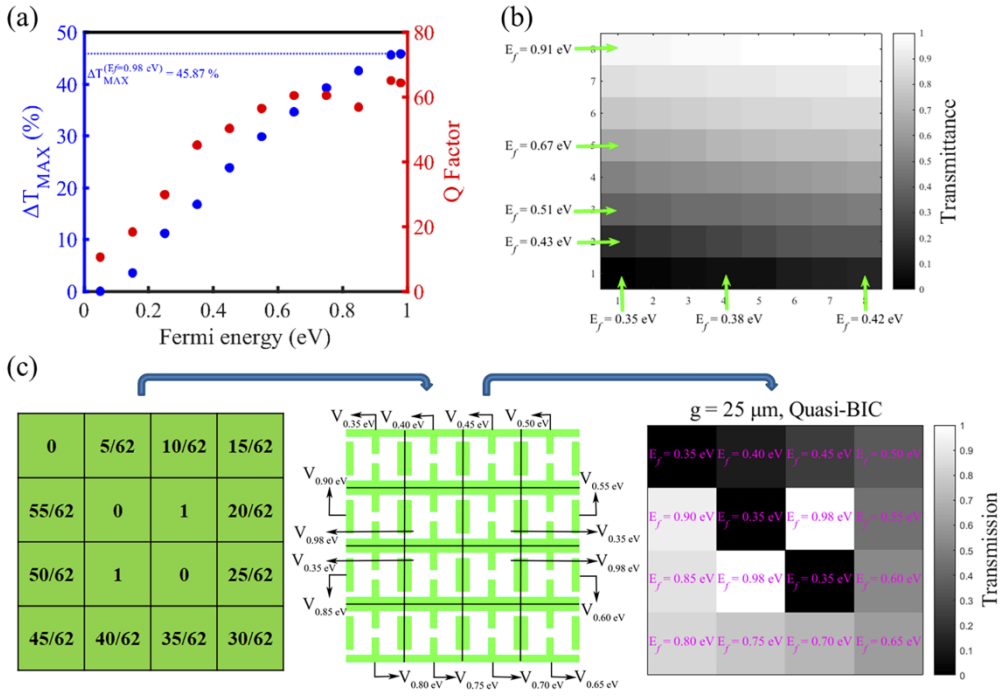

Fig. 6. (a) The amplitude modulation difference and Q factor as a function of the Fermi energy of the DSF metasurface, respectively. (b) Normalized transmission chromaticity plate for 8×8 DSF metasurface array. (c) The process of displaying the chroma intensity in the DSF metasurface pixel array.

Optical Materials EXPRESS

First, normalize the transmission amplitude of the quasi-BIC by setting the value of the resonance amplitude at $E_f = 0.98$ eV to 1 and the amplitude at $E_f = 0.35$ eV to 0. For every 0.01 eV difference in the Fermi energy, the electromagnetic spectrum produces a resonance peak corresponding to chromaticity, and the normalized transmission amplitude is defined as:

$$t_{normal} = (t - t_a)/(t_b - t_a) \tag{7}$$

where t_a is the amplitude of the resonance peak at a Fermi energy of 0.35 eV, t_b is the amplitude of the resonance peak at a Fermi energy of 0.98 eV, and t is the amplitude of the resonance peak at different Fermi energies. In this way, a chromaticity diagram is obtained in Fig. 6(b), where the Fermi energies of 0.35-0.98 eV correspond to 64 normalized chromaticities, respectively. It is theoretically possible to create three-dimensional graphics. The actual implementation is done by treating each unit cell of the DSF metasurface array as a pixel, with each pixel controlled by an applied bias voltage independent of the dielectric constant of the DSM. External circuits control the bias signal, and the bias signal controls each pixel. Figure 6(c) simulates a digital coding with 4×4 pixels. The pre-selected pattern is digitally encoded and then a set of bias signals are generated by the driver circuit. Since the transmission amplitude of the DSF metasurface is controlled independently by the Fermi energy, Fig. 6(c) depicts the simulated display of the chromaticity gradient square ring for the DSF metasurface array with different Fermi energies.

To obtain the dynamic display of the three-dimensional pattern, we investigate the resonance intensity in the near field of the metasurface using the quasi-BIC transmission amplitude after degeneracy from the accidental BIC. The pattern is finally displayed on the receiver plate by irradiating the previously designed composite metasurface array with a THz radiation source,

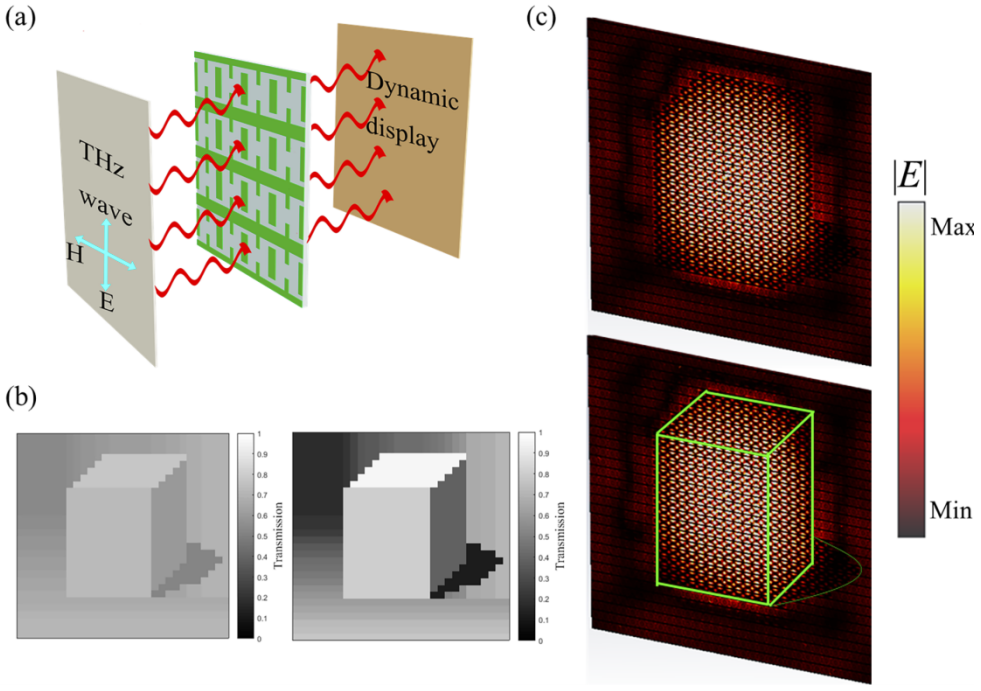

Fig. 7. (a) Dynamic illustration of the transmitted signal model using a THz wave incident on the DSF metasurface array. (b) Numerical simulation of a 30×30 pixel cube (left) and a normalized cube (right). (c) Near-field distribution of the DSF metasurface array simulation experiment.

Optical Materials EXPRESS

as shown in Fig. 7(a). Based on the above principles, we encode a 30×30 DSF metasurface pixel array, write a specific graphics program into a driver circuit that can generate a bias signal, and the driver circuit transmits the bias signal to each metasurface pixel, resulting in each pixel having a specific transmission amplitude and resonance intensity. Figure 7(b) shows the specific stereoscopic squares excited by the numerically simulated DSF metasurface array. On the left is the unnormalized chromaticity diagram, which is closer to the dynamic representation of a real image, and on the right is the normalized chromaticity diagram, which makes discrimination of chromaticity clearer. Figure 7(c) shows the near-field distribution when an electromagnetic wave of 0.5424 THz is incident on the DSF metasurface. The electric field intensity of the quasi-BIC state exhibits significant differences depending on the different Fermi energies of the DSFs. For better observation, we have drawn green lines to indicate the positions of the cubes and their shadows. We can see that each partition has a unique transmission resonance intensity, resulting in a unique chromaticity. Thus, the in-plane cube is clearly shown in the figure, and this research extends the dimensionality for the image representation of the digital encoding of the metasurface.

4. Conclusions

In this study, we propose two types of tunable BICs based on Dirac semimetallic metasurface in the THz band. The symmetry-protected BIC is achieved by breaking the structural symmetry, and the accidental BIC is achieved by tuning the parameters, and the Q factor of the corresponding quasi-BIC can be up to about 175. To better understand the excitation mechanism of the quasi-BIC, we investigated the magnetic field distribution and current distribution of the BIC and quasi-BIC, respectively. The results showed that the accidental BIC and the symmetry-protected BIC have a common resonance mode, and the two LC resonance modes are coupled with each other, which causes a strong resonance. It is significant that the active Q tuning and dynamic amplitude modulation of the quasi-BIC are achieved by adjusting the Fermi energy of the DSM, and the difference in amplitude modulation can reach 46%. Moreover, the transmission amplitude modulation of the DSF metasurface-supported quasi-BIC can be used for the dynamic display of planar stereo images in the THz band, and different stereographies can be achieved by applying bias signals to each structure without varying the parameters of the metasurface structure.

Funding. National Natural Science Foundation of China (61875106, 62105187); Natural Science Foundation of Shandong Province (ZR2021QF010).

Disclosures. The authors declare no conflicts of interest.

Data availability. Data underlying the results presented in this paper are not publicly available at this time but maybeobtained from the authors upon reasonable request.

References

1. Y. Liu, W. Zhou, and Y. Sun, "Optical refractive index sensing based on high-Q bound states in the continuum in free-space coupled photonic crystal slabs," Sensors **17**(8), 1861 (2017).
2. S. Romano, G. Zito, S. Torino, G. Calafiore, E. Penzo, G. Coppola, S. Cabrini, I. Rendina, and V. Mocella, "Label-free sensing of ultralow-weight molecules with all-dielectric metasurfaces supporting bound states in the continuum," Photonics Res. **6**(7), 726 (2018).
3. F. Yesilkoy, E. R. Arvelo, Y. Jahani, M. Liu, A. Tittl, V. Cevher, Y. Kivshar, and H. Altug, "Ultrasensitive hyperspectral imaging and biodetection enabled by dielectric metasurfaces," Nat. Photonics **13**(6), 390–396 (2019).
4. T. Wang and X. Zhang, "Improved third-order nonlinear effect in graphene based on bound states in the continuum," Photonics Res. **5**(6), 629 (2017).
5. T. Wang and S. Zhang, "Large enhancement of second harmonic generation from transition-metal dichalcogenide monolayer on grating near bound states in the continuum," Opt. Express **26**(1), 322–337 (2018).
6. J. M. Foley, J M. Foley, S. M. Young, and J. D. Phillips, "Symmetry-protected mode coupling near normal incidence for narrow-band transmission filtering in a dielectric grating," Phys. Rev. B **89**(16), 165111 (2014).
7. M. L. Vallejo, M. L. L. de Guevara, and P. A. Orellana, "Triple Rashba dots as a spin filter: Bound states in the continuum and Fano effect," Phys. Lett. A **374**(48), 4928–4932 (2010).
8. S. T. Ha, Y. H. Fu, N. K. Emani, Z. Pan, R. M. Bakker, R. P. Domínguez, and A. I. Kuznetsov, "Directional lasing in resonant semiconductor nanoantenna arrays," Nat. Nanotechnol. **13**(11), 1042–1047 (2018).

Optical Materials EXPRESS

9. A. Kodigala, T. Lepetit, Q. Gu, B. Bahari, Y. Fainman, and B. Kanté, "Lasing action from photonic bound states in continuum," Nature **541**(7636), 196–199 (2017).
10. C. M. Watts, X. Liu, and W. J. Padilla, "Metamaterial electromagnetic wave absorbers," Adv. Mater. **24**(23), OP98–OP120 (2012).
11. S. I. Azzam and A. V. Kildishev, "Photonic bound states in the continuum: From basics to applications," Adv. Opt. Mater. **9**(1), 2001469 (2021).
12. C. W. Hsu, B. Zhen, A. D. Stone, J. D. Joannopoulos, and M. Soljačić, "Bound states in the continuum," Nat. Rev. Mater. **1**(9), 16048 (2016).
13. Y. Plotnik, O. Peleg, F. Dreisow, M. Heinrich, S. Nolte, A. Szameit, and M. Segev, "Experimental observation of optical bound states in the continuum," Phys. Rev. Lett. **107**(18), 183901 (2011).
14. C. W. Hsu, B. Zhen, J. Lee, S. L. Chua, S. G. Johnson, J. D. Joannopoulos, and M. Soljačić, "Observation of trapped light within the radiation continuum," Nature **499**(7457), 188–191 (2013).
15. H. Friedrich and D. Wintgen, "Interfering resonances and bound states in the continuum," Phys. Rev. A **32**(6), 3231–3242 (1985).
16. X. Gao, B. Zhen, M. Soljačić, H. Chen, and C. W. Hsu, "Bound states in the continuum in fiber Bragg gratings," ACS Photonics **6**(11), 2996–3002 (2019).
17. A. Taghizadeh and I. S. Chung, "Quasi bound states in the continuum with few unit cells of photonic crystal slab," Appl. Phys. Lett. **111**(3), 031114 (2017).
18. Z. Yu, X. Xi, J. Ma, H. K. Tsang, C. L. Zou, and X. Sun, "Photonic integrated circuits with bound states in the continuum," Optica **6**(10), 1342 (2019).
19. C. L. Zou, J. M. Cui, F. W. Sun, X. Xiong, X. B. Zou, Z. F. Han, and G. C. Guo, "Guiding light through optical bound states in the continuum for ultrahigh-Q microresonators," Laser Photonics Rev. **9**(1), 114–119 (2015).
20. M. F. Limonov, M. V. Rybin, A. N. Poddubny, and Y. S. Kivshar, "Fano resonances in photonics," Nat. Photonics **11**(9), 543–554 (2017).
21. T. Y. Zeng, G. D. Liu, L. L. Wang, and Q. Lin, "Light-matter interactions enhanced by quasi-bound states in the continuum in a graphene-dielectric metasurface," Opt. Express **29**(24), 40177–40186 (2021).
22. Y. K. Srivastava, R. T. Ako, M. Gupta, M. Bhaskaran, S. Sriram, and R. Singh, "Terahertz sensing of 7 nm dielectric film with bound states in the continuum metasurfaces," Appl. Phys. Lett. **115**(15), 151105 (2019).
23. X. Zhao, C. Chen, K. Kaj, I. Hammock, Y. Huang, R. D. Averitt, and X. Zhang, "Terahertz investigation of bound states in the continuum of metallic metasurfaces," Optica **7**(11), 1548 (2020).
24. S. Han, L. Cong, Y. K. Srivastava, B. Qiang, M. V. Rybin, A. Kumar, R. Jain, W. X. Lim, V. G. Achanta, S. S. Prabhu, Q. J. Wang, Y. S. Kivshar, and R. Singh, "All-dielectric active terahertz photonics driven by bound states in the continuum," Adv. Mater. **31**(37), 1901921 (2019).
25. D. Liu, F. Wu, R. Yang, L. Chen, X. He, and F. Liu, "Quasi-bound states in the continuum in metal complementary periodic cross-shaped resonators at terahertz frequencies," Opt. Lett. **46**(17), 4370–4373 (2021).
26. S. Han, P. Pitchappa, W. Wang, Y. K. Srivastava, M. V. Rybin, and R. Singh, "Extended bound states in the continuum with symmetry-broken terahertz dielectric metasurfaces," Adv. Opt. Mater. **9**(7), 2002001 (2021).
27. S. Xiao, T. Wang, T. Liu, C. Zhou, X. Jiang, and J. Zhang, "Active metamaterials and metadevices: A review," J. Phys. D: Appl. Phys. **53**(50), 503002 (2020).
28. E. Mikheeva, K. Koshelev, D. Y. Choi, S. Kruk, J. Lumeau, R. Abdeddaim, I. Voznyuk, S. Enoch, and Y. Kivshar, "Photosensitive chalcogenide metasurfaces supporting bound states in the continuum," Opt. Express **27**(23), 33847–33853 (2019).
29. X. Chen and W. Fan, "Tunable bound states in the continuum in all-dielectric terahertz metasurfaces," Nanomaterials **10**(4), 623 (2020).
30. G. D. Liu, X. Zhai, H. Y. Meng, Q. Lin, Y. Huang, C. J. Zhao, and L. L. Wang, "Dirac semimetals based tunable narrowband absorber at terahertz frequencies," Opt. Express **26**(9), 11471–11480 (2018).
31. Y. Su, Q. Lin, X. Zhai, X. Luo, and L. L. Wang, "Controlling terahertz surface plasmon polaritons in Dirac semimetal sheets," Opt. Mater. Express **8**(4), 884 (2018).
32. C. Ma, Q. Lin, L. Wang, and K. Huang, "Highly tunable dual bound states in the continuum in bulk Dirac semimetal metasurface," Appl. Phys. Express **14**(4), 042002 (2021).
33. Z. Huang, G. Liu, and L. Wang, "Active modulation of quasi-bound state in the continuum based on bulk Dirac semimetals metamaterial," Appl. Phys. Express **15**(3), 032006 (2022).
34. T. Wang, M. Cao, Y. Zhang, and H. Zhang, "Tunable polarization-nonsensitive electromagnetically induced transparency in Dirac semimetal metamaterial at terahertz frequencies," Opt. Mater. Express **9**(4), 1562 (2019).
35. H. Chen, H. Zhang, M. Liu, Y. Zhao, X. Guo, and Y. Zhang, "Realization of tunable plasmon-induced transparency by bright-bright mode coupling in Dirac semimetals," Opt. Mater. Express **7**(9), 3397 (2017).
36. L. Dai, Y. Zhang, X. Guo, Y. Zhao, S. Liu, and H. Zhang, "Dynamically tunable broadband linear-to-circular polarization converter based on Dirac semimetals," Opt. Mater. Express **8**(10), 3238 (2018).
37. J. Li, J. Li, C. Zheng, Z. Yue, S. Wang, M. Li, H. Zhao, Y. Zhang, and J. Yao, "Free switch between bound states in the continuum (BIC) and quasi-BIC supported by graphene-metal terahertz metasurfaces," Carbon **182**, 506–515 (2021).
38. O. V. Kotov and E. Lozovik Yu, "Dielectric response and novel electromagnetic modes in three-dimensional Dirac semimetal films," Phys. Rev. B **93**(23), 235417 (2016).

Optical Materials EXPRESS

39. J. Luo, Q. Lin, L. Wang, S. Xia, H. Meng, and X. Zhai, "Ultrasensitive tunable terahertz sensor based on five-band perfect absorber with Dirac semimetal," Opt. Express **27**(15), 20165–20176 (2019).
40. H. Meng, X. Shang, X. Xue, K. Tang, S. Xia, X. Zhai, Z. Liu, J. Chen, H. Li, and L. Wang, "Bidirectional and dynamically tunable THz absorber with Dirac semimetal," Opt. Express **27**(21), 31062–31074 (2019).
41. T. Klein, O. G. Symko, D. N. Davydov, and A. G. M. Jansen, "Observation of a Narrow Pseudogap near the Fermi Level of A1CuFe Quasicrystalline Thin Films," Phys. Rev. Lett. **74**(18), 3656–3659 (1995).